Spring 4-15-2022

Hot Rocks: Constraining the Thermal Conditions of the Mistastin Lake Impact Melt Deposits Using Zircon Grain Microstructures

Gavin Douglas Tolometti
Western University, gtolomet@uwo.ca

Timmons M. Erickson
NASA Johnson Space Center

Gordon R. Osinski
Western University, gosinski@uwo.ca

Cyril Cayron
Laboratory of ThermoMechanical Metallurgy

Catherine Neish

Citation of this paper:
Tolometti, G. D., Erickson, T. M., Osinski, G. R., Cayron, C., & Neish, C. D. (2022). Hot rocks: Constraining the thermal conditions of the Mistastin Lake impact melt deposits using zircon grain microstructures. *Earth and Planetary Science Letters*, *584*, 117523.

Hot Rocks: Constraining the Thermal Conditions of the Mistastin Lake Impact Melt Deposits Using Zircon Grain Microstructures

G. D. Tolometti[1,2]*, T. M. Erickson[3], G. R. Osinski[1,2], C. Cayron[4], C. D. Neish[1,2]

[1]*Department of Earth Sciences, University of Western Ontario, London, Canada, N6A 5B7*

[2]*Institute for Earth and Space Exploration, University of Western Ontario, Ontario, London, Canada, N6A 5B7*

[3]*Jacobs JETS, ARES division, NASA Johnson Space Center, Mailcode XI3, Houston, TX, 77058, USA*

[4]*Laboratory of ThermoMechanical Metallurgy (LMTM), PX Group Chair, École Polytechnique Fédérale de Lausanne (EPFL), Rue de la Maladière 71b, 2000Neuchâtel, Switzerland*

*Corresponding Author: gtolomet@uwo.ca

Abstract

The production of superheated melt during hypervelocity impact events has been proposed to be a common occurrence on terrestrial planetary bodies. Recent direct evidence of superheated impact melt temperatures exceeding >2370°C from the Kamestastin (Mistastin Lake) impact structure, Canada, was based on a single impact glass sample. Such high superheated melt temperatures have strong implications for the evolution of crustal material, the thermal history of impact cratering events, and the rheology of impact melt. However, although widely predicted in previous studies, with the exception of the Mistastin Lake impact glass, there is little direct evidence for superheated temperatures in multiple settings across an impact structure. Therefore, an outstanding question is how heterogeneous are superheated conditions across a single impact structure. In this work, we analyze the crystallographic orientations and microstructures of zircon grains and the precursor parent phases of baddeleyite crystals, from four different samples representing the entire melt-bearing stratigraphy at Mistastin: an impact glass, a vesicular clast-poor impact melt rock, a clast-rich impact melt rock, and a glass-bearing impact breccia. Using electron microprobe analysis followed by electron backscatter diffraction, we discovered that four zircon grains with vermicular coronae of baddeleyite crystals from the impact glass contain evidence for a cubic zirconia precursor, indicative of temperature conditions >2370 °C. We also report evidence of superheating up to 1673 °C in the glass-bearing impact breccia. In addition, we also report the first occurrence at Mistastin of the high-pressure zircon polymorph reidite and former reidite in granular neoblastic (FRIGN) zircon in grains from the glass-bearing impact breccia, implying minimum peak shocks from 30–40 GPa. The identification of superheating from two localities at Mistastin demonstrates (1) that superheating is not restricted solely to rapidly cooled impact melt rock samples and is therefore more

distributed across impact structures, and (2) we can investigate the P-T evolution pathways of impact melt from different impact settings, providing a clearer picture of the thermal conditions and history of the impact structure.

1.0 Introduction

Impact cratering is a widespread geologic process throughout the Solar System and has played a critical role in the accretion of planetary bodies (e.g., Melosh, 1989). A common product of impact cratering events is melt, which forms upon decompression of rocks subjected to high shock pressures (>60–100 GPa; e.g., Dence, 1971; Melosh, 1989). Unlike decompression and flux melting that occurs in planetary interiors, impact melting is (1) near instantaneous, (2) a function of shock pressure and the compressibility of target rocks and their constituent minerals, and (3) compositionally controlled by wholescale melting of the target rocks as opposed to the minerals with the lowest solidus temperatures (Grieve et al., 1977; Melosh, 1989; Osinski et al., 2018). Evidence for melting of refractory minerals at temperatures >1400–1800° C (such as rutile and zircon; Dressler et al., 1987; El Goresy, 1968, 1965), led to the hypothesis that impact melts were superheated. In this context, superheated means that the melt experienced temperatures well above the liquidus. At such temperatures (e.g., >1000°C for felsic compositions and >1200°C for mafic compositions), impact melt would behave as a Newtonian fluid, exhibiting a viscosity that remains constant until sufficient cooling has commenced (Chhabra, 2010). The temperature of impact melt is, therefore, a key physical property for understanding the formation and emplacement of impact melt deposits (e.g., Lev et al., 2021; Osinski et al., 2011), and the evolution of impact melt composition and cooling rates; which have implications for understanding impact-induced hydrothermal systems and the solubility of

elements essential for crustal differentiation. It also can provide critical information on how impact cratering processes modified and devolatilized the early Earth's and Moon crustal material (Gomes et al., 2005; Kring and Cohen, 2002; Marchi et al., 2014).

Estimating rock formation temperatures requires preservation of geothermometers, such as compositional endmembers in mineral systems (Hart and Davis, 1978; Lindsley and Andersen, 1983; Sack and Ghiorso, 1991). However, conventional geothermometers are not suitable for estimating the temperatures of superheated impact melt exceeding 1800°C, as these geothermometers only work in thermodynamically equilibrated rocks. Recently, impact melt temperatures have been constrained by examining the crystallographic orientation relationships of accessory minerals that can record hypervelocity impact conditions (e.g., Cavosie et al., 2016; Erickson et al., 2019; Timms et al., 2017a; White et al., 2020) . Two accessory minerals used to constrain both impact melt temperatures and shock pressures are baddeleyite (i.e., monoclinic zirconia (ZrO_2)) and zircon ($ZrSiO_4$). Superheated temperatures can be constrained by documenting orientation relationships in baddeleyite crystals (El Goresy, 1965; Kaiser et al., 2008; Timms et al., 2017a; White et al., 2018), which are a dissociation product of zircon at temperatures above 1673 °C at atmospheric pressure. Zircon is a durable accessory mineral that can record both temperature (to an extent) and pressure conditions (Cavosie et al., 2016; Kusaba et al., 1985; Wittmann et al., 2006).

Previous work by Timms et al. (2017b) discovered zircon grains with coronae of baddeleyite crystals that had back transformed from cubic zirconia in an impact glass sample from the Mistastin Lake (known locally to the Innu as Kamestastin) impact structure, Newfoundland and Labrador, Canada. Evidence for the cubic zirconia polymorph transformation implies superheated temperatures >2370 °C at near surface/ambient conditions (cf. Kaiser et al.

2008); this is the highest recorded formation temperature for any crustal rock on Earth. In addition, a recent study by White et al. (2020) discovered a ~250 μm, subhedral baddeleyite grain with similar systematic orientations indicative of cubic zirconia phase heritage in coarse grained lunar troctolite 76353. The baddeleyite grain analyzed by White et al. (2020) is purported to have been entrained in superheated melt generated from a basin-forming impact event, suggesting hypervelocity impacts on the Moon, and potentially other rocky planetary bodies, produce superheated impact melts. In addition to impact melt deposits, melting in an impact structure can occur through the partial melting of target material by thermal erosion and from collapse of crater walls (Melosh and Ivanov, 1999). A question therefore stands, how widespread is evidence for superheating in different melt settings within a single impact structure? If superheating is common on a crater-scale, then evidence for high temperature melt conditions may be widely distributed within single impact structures, and preserved within a diverse array of impactite samples.

In this work, we analyzed zircon and zirconia from a diverse suite of impactites from the Mistastin Lake impact structure (Fig. 1). The impactites selected include a sample of the same type of impact glass studied by Timms et al. (2017b), in addition to a clast-poor vesicular impact melt rock, a clast-rich impact melt rock, and a glass-bearing impact breccia (Figs. 1C-F). Each of the analyzed samples were selected to represent a different unit within Mistastin's impactite stratigraphy as described from field observations and petrographic analysis (Grieve, 1975; Mader and Osinski, 2018).

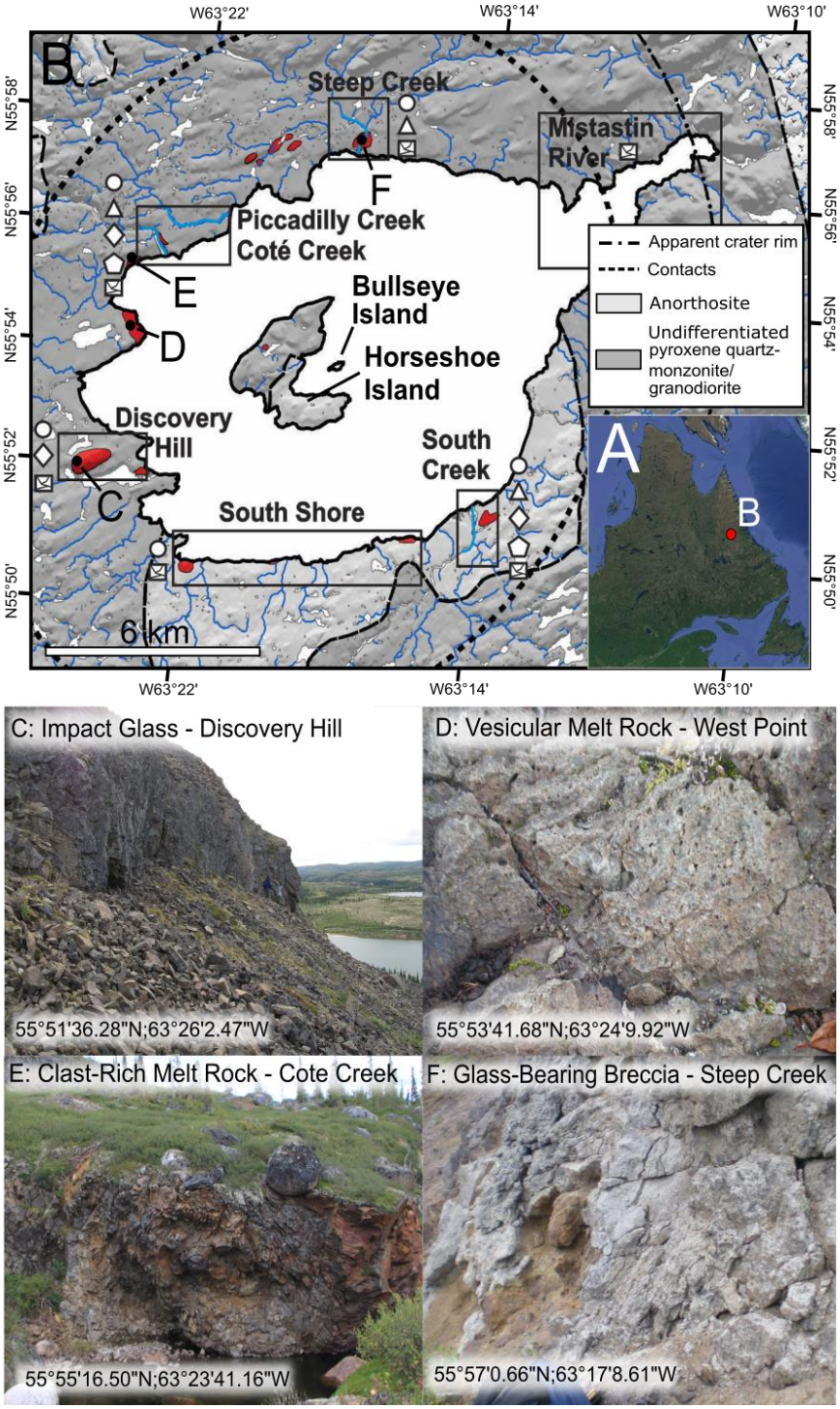

Figure 1. (A) Location of the Mistastin Lake impact structure in Labrador, Canada (55.8833° N; 63.3333°W). (B) Geologic map of Mistastin modified from Mader and Osinski (2018), showing the locations of the impactite samples. Red polygons represent impact melt deposits mapped by Currie (1971), Grieve (1975), and Marion and Sylvester (2010). Locations of the impactites studied here are Discovery Hill (C), West Point (D), Cote Creek (E) and Steep Creek (F).

1.1 Geologic Setting

Mistastin is a 28-km diameter, 37.83 ± 0.05 Ma (Sylvester et al., 2013) complex impact structure formed in a target of Na-anorthosite, granodiorite, and quartz monzonite (Grieve, 1975; Marion and Sylvester, 2010). The impact structure is situated within the northeastern region of the Mesoproterozoic Mistastin Batholith, made primarily of anorthositic and granitic rocks with minor amounts of gabbroic rocks. Within the center of Mistastin is a near circular lake, occupying the inner 16 km diameter of the crater (Fig. 1B). Two islands, Horseshoe Island and Bullseye Island, are located near the center of Mistastin. These islands are interpreted to be the remnants of a central uplift (Marion and Sylvester, 2010), which has since been eroded by glacial processes. The majority of the impact melt deposits are found along the western margin of the lake, with a few small outcrops also present on Horseshoe Island and along the south and southeastern shoreline (Fig. 1B).

The impactite deposits around the structure have varying proportions of impact melt. Grieve (1975) and Mader and Osinski (2018) describe these impactites in a structured impactite stratigraphy (generalized example in Fig. 2), from the base upwards: unshocked target → fractured and shocked target rocks → monomict impact breccias → polymict impact breccias → impact melt rocks (increase in grain size and decrease in clast abundance from bottom to top) (Figs. 2A-D). The lowermost melt-bearing impactites are allochthonous glass-bearing impact breccias (Figs. 1F and 2D), which overlie melt-free monomict and polymict lithic clastic breccias. Some of the glass-bearing impact breccias are found as impact dykes that intruded into melt-free and melt-poor breccias and shocked target rocks. Moving up the stratigraphy, the glass-bearing breccia transitions to clast-rich impact melt (Figs. 1E and 2C). The contact zone between

these two impactites is 1–3 m thick, with sinuous and amoeboid shaped lenses of the two impactites intermingling with each other (Mader and Osinski, 2018). Further up the impactite stratigraphy, the clast-rich impact melt unit transitions to a fine to medium-grained clast-poor impact melt rock. At this transition, the abundance of clasts decreases from >15% to <10% and, at the West Point locality the melt rock is vesicular (Fig. 1D).

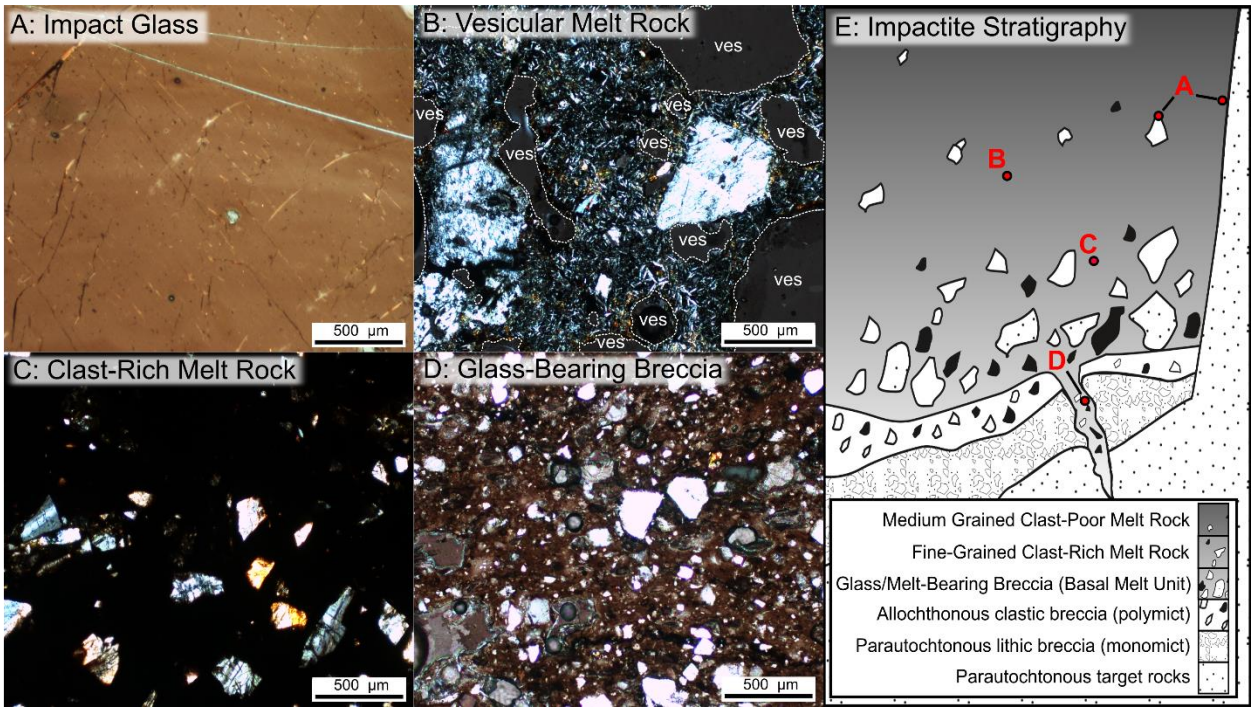

Figure 2. Petrographic images of the four impactite samples and their spatial relation in the impactite stratigraphy described by Grieve (1975) and Mader and Osinski (2018). (A) Plane-polarized light (PPL) image of the deep brown hyaline impact glass. (B) Vesicular clast-poor melt rock showing a matrix comprising elongate plagioclase crystals. White dashed lines outline the margins of the vesicles (ves). Clasts of quartz and plagioclase with undulous extinction, annealed boundaries, toasting textures (quartz clasts only) are evenly distributed throughout the entire sample. (C) Aphanitic to fine-grained clast-rich melt rock containing clasts of clinopyroxene, quartz, and plagioclase. Extinction twinning is still visible in the plagioclase under cross-polarized light (XPL). (D) PPL image of the deep brown glass matrix in the glass-bearing impact breccia collected from an impact breccia dyke. Clasts of quartz and plagioclase in the glass matrix are <100 µm and range from sub-rounded to angular in shape. (E) Generalized impactite stratigraphy of Mistastin with annotations marking the inferred origin of the impactite samples. Note the impact glass has two potential locations, along the contact with the crater wall

and as a quenched melt rind surrounding a large clast (sample was not found in-situ, locations on figure are inferred). The impact glass was not collected in-situ so its exact stratigraphic position at the Discovery Hill melt deposit at Mistastin is unknown. Image modified from Osinski et al. (2008).

2.0 Methods

Polished thin sections were prepared from the glass-bearing impact breccia, clast-rich melt rock and clast-poor melt rock, and impact glass sample to identify zircon grains within their glass and crystalline melt matrices. Optical microscopy was used to study the microtextures and mineralogy of the glass/melt matrices of the four impactite samples at the University of Western Ontario Earth and Planetary Materials Analysis (EPMA) Laboratory. A total of 69 zircon grains were identified using electron micro-probe analysis (EMPA) on a JEOL JXA-8530F field emission electron microprobe at the EPMA laboratory. Grains with dimensions as small as 3 μm were identified. A summary of the grains found in each impactite sample and their size dimensions are reported in Table 1. A backscattered electron (BSE) image was obtained for each zircon grain to characterize grain morphology, shock metamorphic features, and to identify, if present, evidence of dissociation. Wavelength-dispersive spectroscopy spot analysis was used to analyze the glass and crystalline matrix composition of the impactite samples to determine if they were homogenous. After EMPA, the polished thin sections were prepared for electron backscatter diffraction (EBSD) analysis. Each thin section was further polished using a 50 nm colloidal silica dispersion in NaOH for three hours on a Buehler Vibromet II polisher. Finally, a 5 Å-thick carbon-coat was applied to each polished thin section to mitigate electron charging on the surface during EBSD analysis.

Crystallographic orientation maps of the zircon grains were obtained using a JEOL 7600F field emission Scanning Electron Microscopy (SEM) instrument in the E-beam analytical suite of the Astromaterials Research and Exploration Science division at the Johnson Space Center, Houston, TX, USA. The operation conditions were optimized in the SEM for EBSD analysis, including a stage tilt of 70° relative to the incident angle of the electron beam, an acceleration voltage of 20 kV, a beam current of 10 nA, and a 50 – 250 nm step size (Erickson et al., 2021). The microstructures of the zircon grains were analyzed using forescatter electron (FSE) imaging and EBSD mapping. Electron backscatter diffraction patterns were collected using an Oxford Instruments Symmetry detector. The phase and orientations of individual EBSD patterns were indexed using match units based on the 1 atm unit cell of Hazen & Finger (1979) for zircon, the unit cell of Howard et al. (1988) for baddeleyite, and 0.69 GPa unit cell of Farnan et al. (2003) for reidite. The EBSD data were processed using Oxford's Channel5 program suite; phase and orientation maps were produced using Tango and pole figures were produced using Mambo. To confirm if any of the coronas of baddeleyite preserved the cubic to monoclinic zirconia transformation, we reconstructed their EBSD orientation data using the Python based ARPGE phase reconstruction software (Cayron, 2007).

3.0 Results

3.1 Impactite Petrography

The impact glass sample has a deep brown to black hyaline matrix (Fig. 2A). The glass contains clasts of extensively fractured and toasted quartz and fractured plagioclase, all exhibiting undulous extinction under cross-polarized light. At the macro-scale (hand specimen) the impact glass matrix appears homogenous. However, we discovered using EMPA that the matrix is locally heterogenous with flow textures comprising the hyaline glass and schlieren (Supplementary File Item 2, Fig. S2). The hyaline glass has a Na-anorthosite and mangerite composition and the schlieren, compared to the hyaline glass, is depleted in SiO_2, Al_2O_3, and Na_2O, but enriched in MgO and FeO (Supplementary File Item 2, Table S1 and Fig. S2). No zircon grains were found within the schlieren, only in the hyaline glass.

The vesicular clast-poor impact melt rock has a fine to medium-grained crystalline matrix comprising elongate plagioclase crystals (Fig. 2B). Clasts of quartz and plagioclase exhibit low to no shock metamorphic features and the vesicles in the melt have an average size of 1 cm.

The clast-rich melt rock is an aphanitic to fine-grained melt matrix with 15% abundance of clasts. Mineral clasts of clinopyroxene, quartz and plagioclase exhibit extensive fracturing (Fig. 2C) and undulous extinction under cross-polarized light.

The glass-bearing impact breccia has a clastic matrix containing particles and pockets of impact glass exhibiting a deep brown colour under plane polarized light (Fig. 2D). The clast

abundance is >25 %, with the glass matrix containing numerous sub-rounded to angular fragments of quartz and plagioclase, most exhibiting undulous extinction and irregular fractures.

Table 1. Number of Zircon Grains

Impactite	No. of Zircon Grains	Zircon Grain Width/Length Dimensions	
Impact Glass	45	3 – 40 μm	8 – 130 μm
Glass-Bearing Breccia	16	10 – 25 μm	15 – 40 μm
Vesicular Clast-Poor Melt Rock	4	10 – 40 μm	20 – 75 μm
Clast-Rich Melt Rock	4	10 – 55 μm	15 – 90 μm

Table 1. Summary of zircon grain and zirconia crystals with size dimensions and total number of identified samples in each impactite.

3.2 Microstructure and Crystallographic Analysis

3.2.1 Glass-Bearing Impactites

3.2.1.1 Impact Glass

We identified a total of 45 zircon grains in the hyaline impact glass sample, 17 (37.8%) of which have vermicular coronas of baddeleyite crystals. The width/length dimensions of the zircon grains range from 3 – 40 μm/8 – 130 μm (Table 1) and the zirconia crystals width/length dimensions range from <0.5 – 3 μm/<1 – 10 μm. From the 45 zircon grains, 22 (48.9%) display no diagnostic features indicative of ZrO_2-SiO_2 dissociation or shock metamorphism. Instead, they exhibit irregular fractures and anhedral crystal shapes (Fig. 3A). Shock twinning was observed in one zircon grain (2.2%) showing {112} twin lamellae, oriented sub-vertical along the grain (see red arrows in Fig. 3B). The grain also exhibits crystal-plastic microstructural

deformation, and cumulative plastic strain ranging up to 23°. From the 17 zircon grains with vermicular coronae of baddeleyite (Fig. 3C), seven exhibit systematic orientations indicating a transformation of cubic to monoclinic zirconia, potentially by a two-stage process via tetragonal zirconia (Cayron et al., 2010). The zircon cores show no diagnostic shock metamorphic features, only low angle boundaries (misorientations <10 °) (see EBSD Texture Component maps in Fig. 3A-C). One zircon grain with a vermicular corona of baddeleyite exhibits granular textures with small <1 μm grains of zirconia inclusions within the granular core (Fig. 3D). EBSD analysis of the zircon neoblasts in the granular core reveals clear 90° misorientations that align with the $<110>_{zircon}$ direction (see Supplementary File, Item 3, Fig. S3). These misorientations are hallmarks for the previous existence of the high pressure polymorph reidite, making this granular core a former reidite granular core (e.g., Former Reidite In Granular Neoblastic (FRIGN) zircon (Cavosie et al., 2018)). In addition, the FRIGN zircon grain records ~65° disorientation relationships about the $<110>_{zircon}$ with alignments of both {110} and {112} between two domains with similar oriented neoblasts (see Supplementary File, Item 3 Fig. S3). These microstructural hallmarks are indicative of {112} twinning, suggesting that in addition to reidite, some of the granules nucleated from deformation twins.

Five of the 45 (11.1%) zircon grains completely dissociated to zirconia (Fig. 3E) and no evidence of preserved silica polymorphs was discovered using EMPA. We also analyzed the crystallographic orientations of the five fully dissociated grains to determine if cubic → monoclinic zirconia transformation occurred. Our results show that none of the fully dissociated grains exhibit the orientation relationships indicative of a cubic zirconia parent grain. The size of the fully dissociated zircon grains range from 23 μm to 50 μm, and the average size of all the zircon grains (dissociated and non-dissociated) in the impact glass sample is 57.5 μm. Due to

their sizes, it is challenging to determine if the dimensions of these grains are idiomorphic to the original zircon or whether they are a 2D slice of a corona of baddeleyite that was cut during polished thin section preparations. The fully dissociated zircon grain sizes are similar to a majority of the grains in the impact glass sample (see Supplementary File Item 1, Fig. S1), with most zircon grains ranging from 20 µm to 60 µm (in length). Since their sizes are similar, it is possible they are remnants of fully dissociated grains.

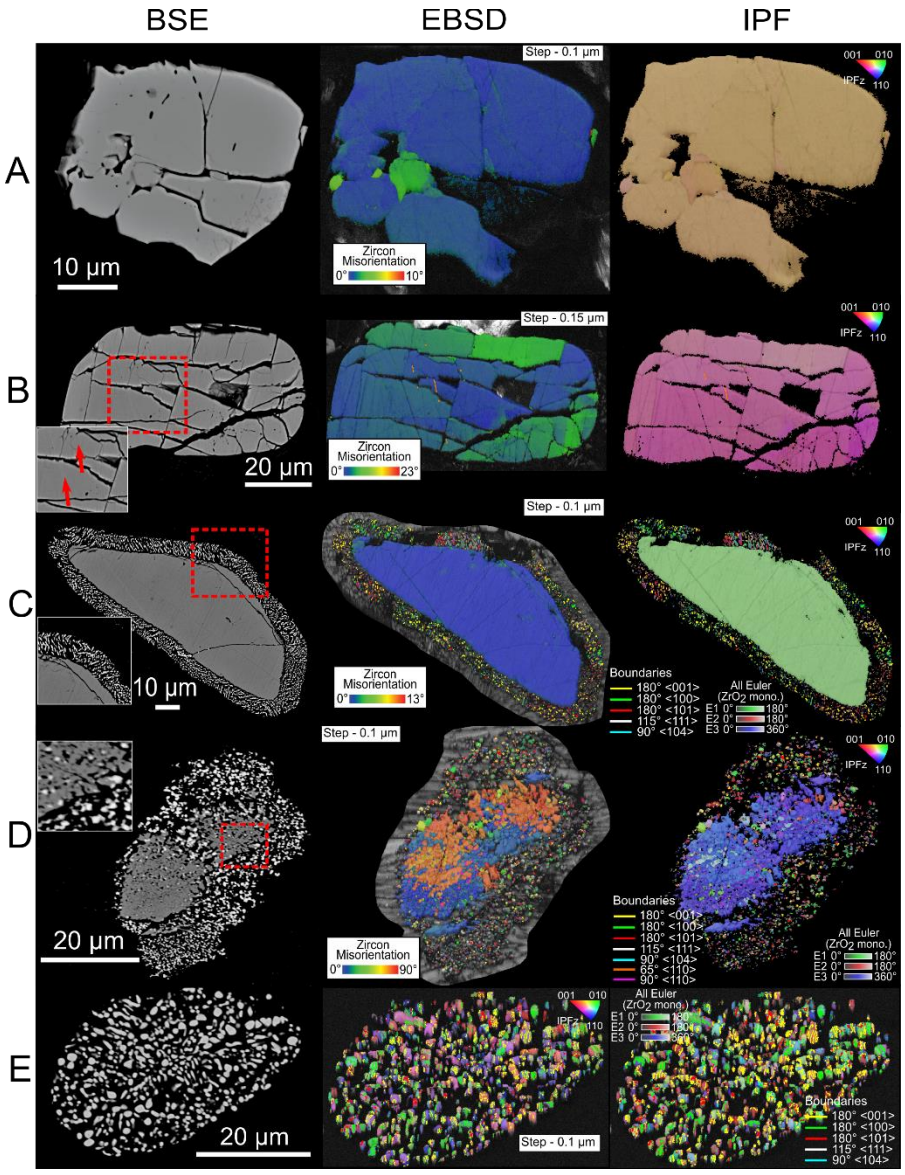

Figure 3. Overview of the zircon grain textures identified in the impact glass sample. Left column shows backscatter electron images of the grains (locations of zoomed images of specific

grain textures outlined by red dashed lines in BSE images), the center column shows EBSD zircon texture component maps, and the right column shows the inverse pole figure (IPF) orientations of each zircon grain and detected zirconia crystals acquired from EBSD analysis. Zircon orientations are assigned the IPF colour scheme and zirconia crystals are assigned Euler plots. (A) Anhedral zircon grain with irregular fractures cross-cutting the center. (B) Zircon grain with evidence of shock twinning ({112} twin lamellae); visible sub-vertical planar fractures cross-cutting the grain (red arrows pointing to subvertical planar fractures cross-cutting grain). (C) Zircon grain with a ~5 μm thick vermicular corona of baddeleyite crystals. (D) A granular zircon grain surrounded by a vermicular corona of baddeleyite with thickness ranging from 2 μm – 10 μm. Zirconia crystals are also found as inclusions within individual granules, in addition to small voids filled with the surrounding silicate glass. (E) Fully dissociated zircon grain with elongate and globular zirconia. No crystalline silica phases were detected in the EMPA and EBSD data.

Figure 4 shows one of the seven zircon grains with vermicular coronas of baddeleyite that exhibit systematic orientation relations indicative of cubic to monoclinic zirconia transformation. The zircon core shows minor disorientations (minimum misorientation) less than 7° (Fig. 4B). The core is elongate, up to ~30 μm long and 5 – 10 μm wide and is surrounded by a 1 – 8 μm thick corona of baddeleyite crystals ranging in size from <0.5 μm – 2 μm wide and up to 5 μm long. The baddeleyite crystals exhibit two distinct morphologies: elongate and sub-rounded, which may either represent different growth habits of baddeleyite crystals or 2D (i.e., basal and prismatic) slices of the same crystal morphology. Using the ARPGE Python-based program, we reconstructed the clusters of baddeleyite crystals to cubic zirconia using the measured EBSD orientation data and theoretical orientation relationships of cubic to tetragonal to monoclinic zirconia transformations reported by Cayron et al. (2010). The misorientations between the baddeleyite crystals were analyzed in detail because they exhibit 90°, 115°, and 180° disorientation angles that are consistent with cubic-monoclinic transformation twinning (Timms et al., 2017b) (Fig. 4D). The pole figures of the baddeleyite crystals (see $<100>_{mono}$ i, ii and iii in Fig. 4E) and reconstructed cubic zirconia crystals (see $<100>_{cubic}$ i, ii and iii in Fig. 4E) show three distinct clusters. These clusters are composed of twelve unique crystallographic

orientation variants that form ~20° cross-shaped patterns on pole figures <100>. Each cluster is spatially distinct, and orthogonal with a ~90° disorientation. This is consistent with the phase transformation from a cubic zirconia parent crystal (Cayron et al., 2010; Timms et al., 2017a,b). Out of the seven zircon grains with vermicular coronas of baddeleyite, four returned positive results confirming cubic → monoclinic zirconia. The other three grains returned less variants of the <100>mono directions (see Fig. 4). A tetragonal parent phase would return a single cluster of <100> variants, and for orthorhombic zirconia, variants in <100> and <010> are not symmetrical equivalents, so we would not produce the orthogonal pattern indicative of tetragonal to monoclinic zirconia.

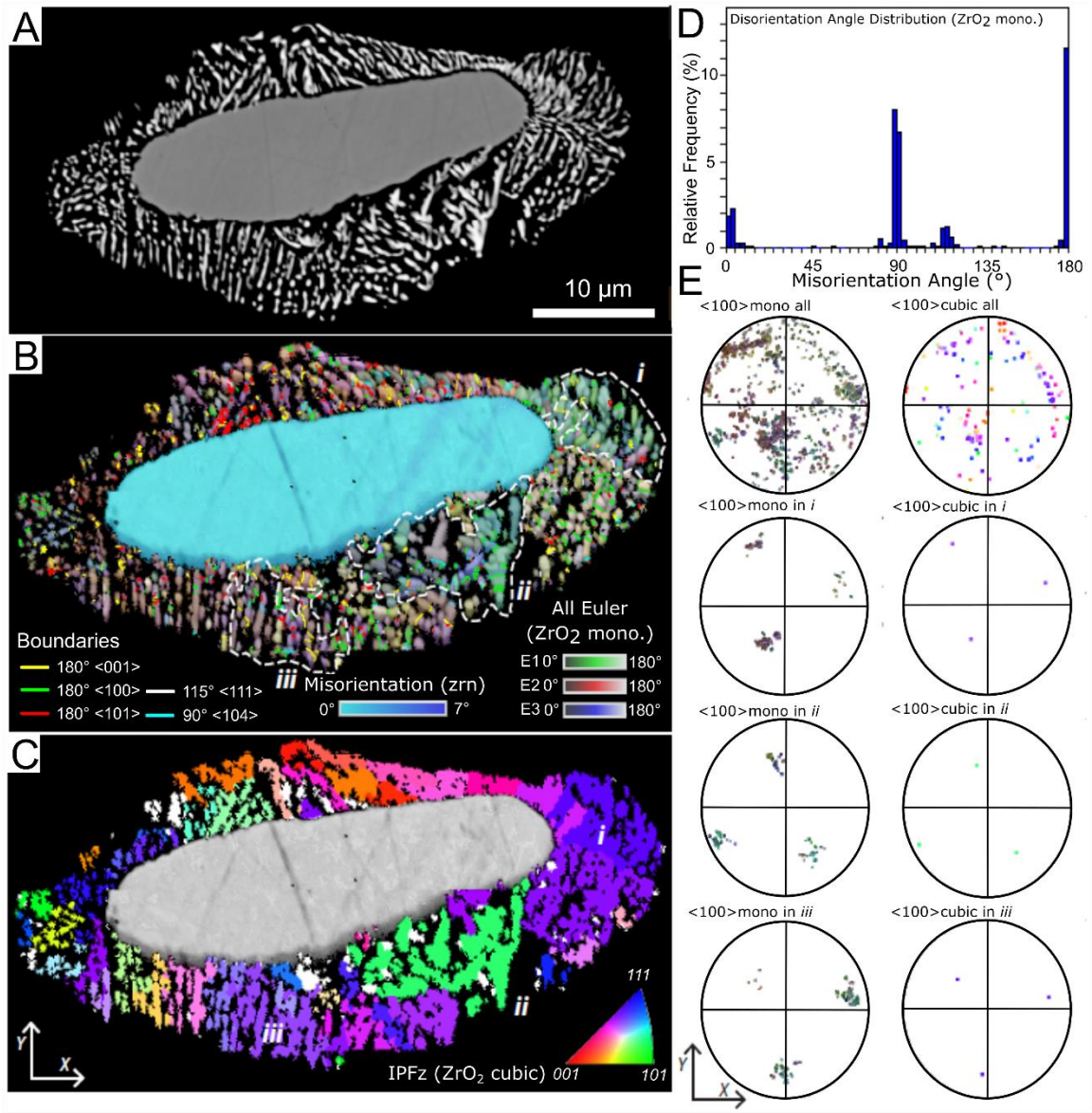

Figure 4. Phase reconstruction of one of four zircon grains (CM09_05A-2) from the impact glass sample with crystallographic evidence of cubic zirconia within the corona of zirconia. (A) BSE image and (B) EBSD orientation map of the zircon grain. (C) Inverse pole figure (IPF) reconstruction of cubic zirconia within the corona using theoretical cubic → monoclinic transformations (Cayron et al. 2010). (D) Histogram of the disorientation angle distribution in the baddeleyite crystals; systematic 90°, 115°, and 180° disorientations are consistent with a cubic parent. (E) Pole figures with <100> baddeleyite and reconstructed <100> cubic zirconia orientations from three baddeleyite domains in the corona.

3.2.1.2 Glass-Bearing Breccia

In the glass-bearing breccia sample, we identified 16 zircon grains, two of which (12.5%) are polymineralic inclusions in a quartz clast while the rest are in contact with the melt matrix. The zircon grains in this sample have sizes ranging from 10 μm – 80 μm (Table 1). The majority of the grains are anhedral with minor brittle deformation and preserve low angle disorientations (misorientations, 0° – 20°) (e.g., Figs. 5A-B). Four of the 16 zircon grains (25%) exhibit granular zircon textures, three of which also contain domains of reidite (example of reidite, Fig. 5C, and example of fully granular grain, Fig. 5D). This is the first discovery of reidite at Mistastin.

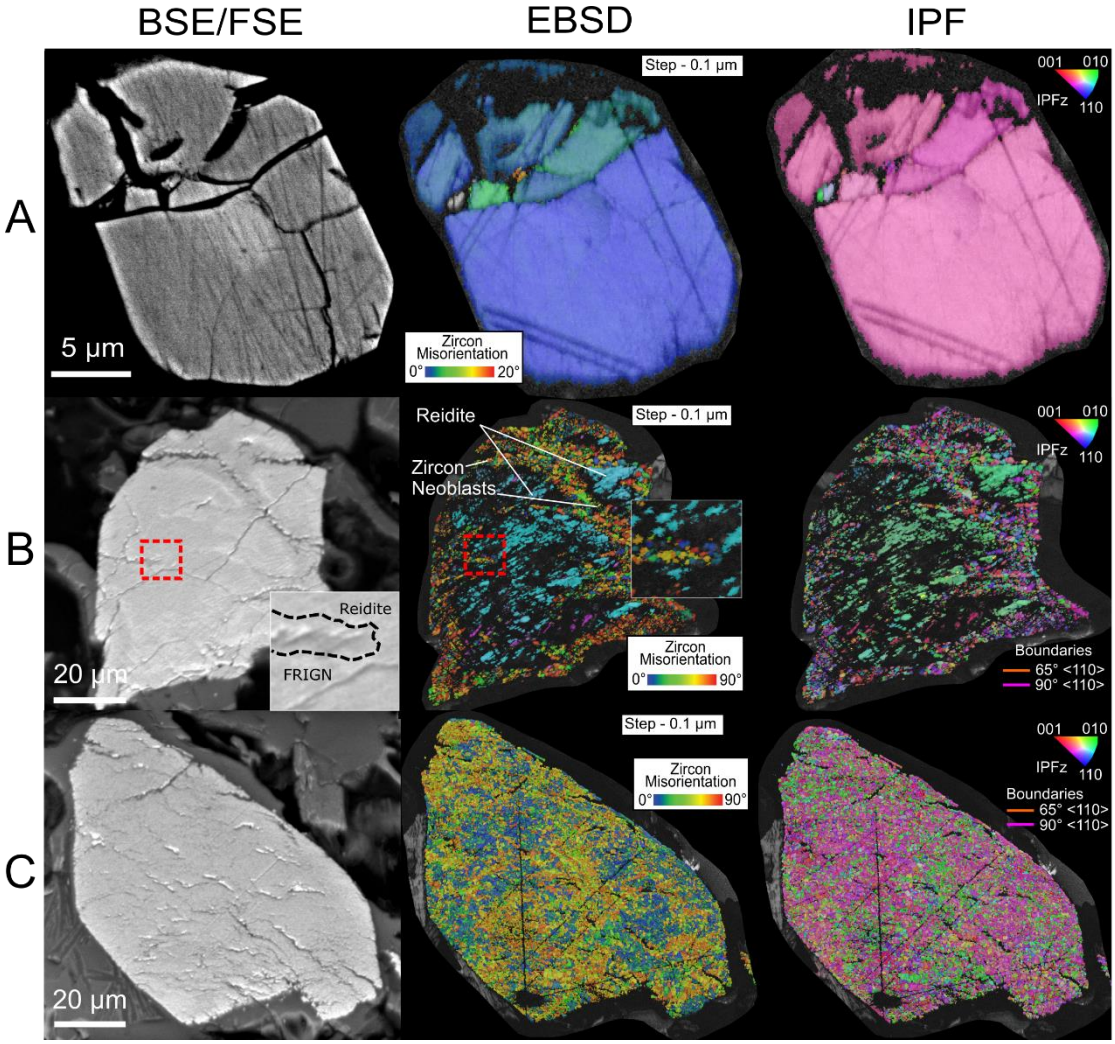

Figure 5. Overview of the zircon grain textures identified in the glass-bearing breccia sample. Left column shows backscatter electron (BSE) or forescatter electron (FSE) images of the grains, the center column shows EBSD zircon texture component maps, and the right column shows the inverse pole figure (IPF) orientations of the zircon grain acquired from EBSD analysis. (A) Subhedral zircon grain with cross-cutting irregular fractures. (B) A domain of high-pressure zircon polymorph reidite surrounded by granular neoblastic zircon grains, which exhibit systematic orientation relationships indicative of the reversion process from reidite to zircon. Special orientation boundaries in zircon shown as coloured lines. (C) A fully granular zircon grain found in close proximity to the three granular, reidite-bearing zircon grains. Orientation relationship data, revealed from EBSD analysis, suggest this granular zircon crystallized from a zircon grain that contained reidite domains. Special orientation boundaries in zircon shown as coloured lines.

The reidite-bearing granular zircon grains exhibit systematic 90° disorientation relationships between $<001>_{zircon}$ and $<110>_{zircon}$ in the neoblasts (Fig. 6) (other examples in

Supplementary File, Item 4, Figs. S4-5). This disorientation and alignment has previously been interpreted as evidence for the reversion of reidite to zircon (Cavosie et al., 2016; Timms et al., 2017a). Our study is one of few to report this reversion product in a granular zircon grain still containing reidite (cf. Erickson et al., 2021, 2017; Plan et al., 2021; Timms et al., 2017a). The reversion from reidite to zircon is also supported by the alignment between the $<110>_{reidite}$ and $<001>_{zircon}$ (Figs. 6D-E).

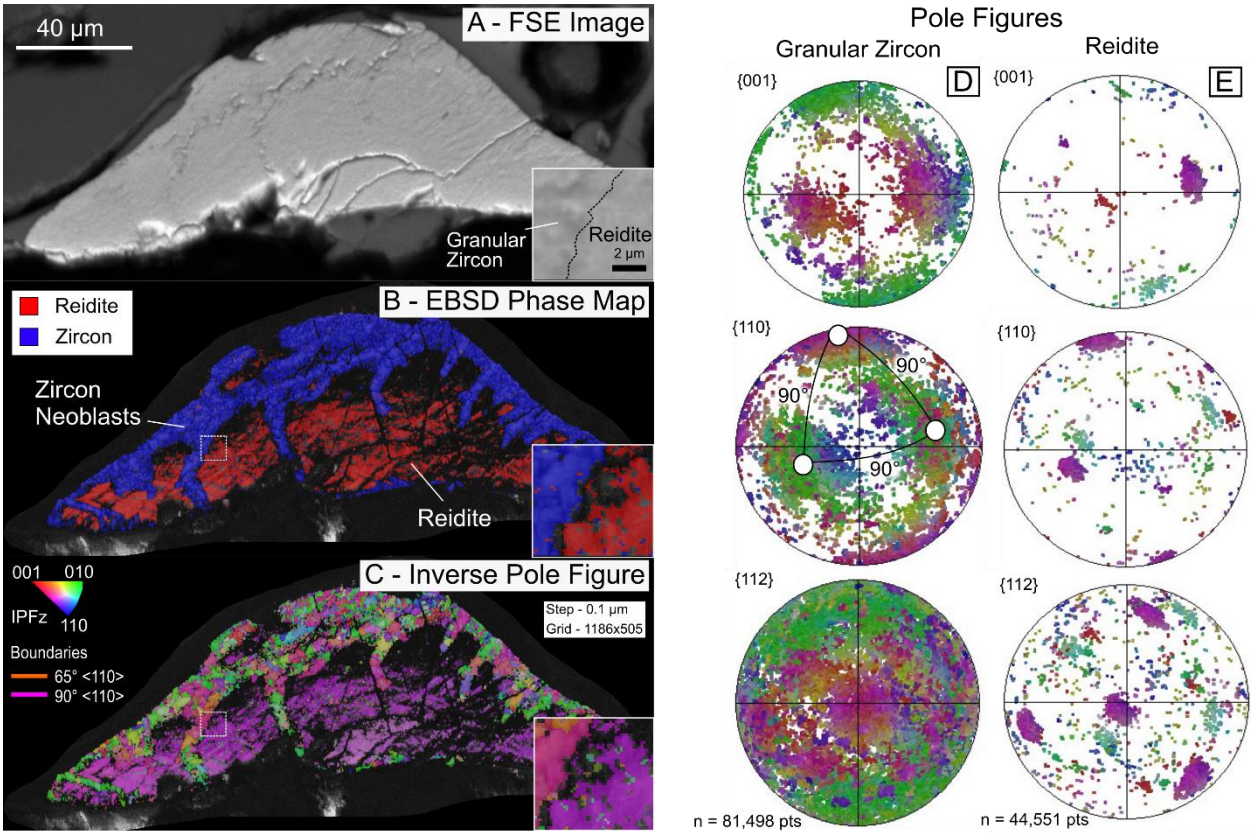

Figure 6. Microstructure and crystallographic orientation data of one of the three reidite-bearing granular zircon grains (sample MM09_033A2-21) from the glass-bearing breccia sample. (A) Forescatter electron (FSE) image of the reidite-bearing granular zircon grain. (B) Electron backscatter diffraction analysis (EBSD) phase map identifying zircon and reidite in the grain. (C) EBSD orientation map of the measured orientations of each zircon neoblast and reidite grain. Zircon and reidite assigned the inverse pole figure (IPF) colour scheme. (D) Pole figures for zircon. Colour scheme as in C. (E) Poles figures for reidite. Colour scheme as in C. Alignment of

grouped variants in $<001>_{zircon}$ and $<110>_{reidite}$ (black circles), and the 90° disorientation relations (as annotated in $<110>_{zircon}$ pole figure) in $<110>_{zircon}$ indicate the granular zircon formed from the reversion process of reidite to zircon.

We also observed a fully granular zircon grain (Fig. 5D). The data from this grain reveals 65° disorientation relationships about the $<110>_{zircon}$ (Supplementary File, Item 5, Fig. S6), which is unique to {112} twinning, similar to the shock twinning observed in the zircon grain in the impact glass sample (Fig. 3B). We also observe systematic 90° disorientation relationships between $<001>_{zircon}$ and $<110>_{zircon}$, similar to what we observe between the reidite and zircon neoblasts in the reidite-bearing granular zircon grains. These alignments and orientation relations are similar to crystallographic relationships connected to the transformation of zircon to reidite and then reversion of reidite to zircon, where the $<001>_{zircon}$ is parallel to the $<110>_{reidite}$, creating two orthogonal sets containing eight unique orientation variants (Erickson et al., 2017). When reidite reverts to zircon it follows orientation relationship paths that produce three approximately orthogonal orientations of zircon (cf. Erickson et al., 2017; Plan et al., 2021; Timms et al., 2017a), showing ~90° disorientations. This confirms that this granular grain is a FRIGN zircon, similar to the FRIGN zircon core identified in the impact glass sample (Fig. 3D).

3.2.2 Crystalline Melt Rock Impactites

3.2.2.1 Vesicular Clast-Poor Impact Melt Rock

Only four zircon grains were discovered in the clast-poor vesicular melt and none had evidence of dissociation. The grains range in size from 10 μm – 75 μm (Table 1). The zircon grains preserve low angle disorientations in their cores, ranging from 0° – 10°. The grains also

391 have voids containing the surrounding silicate melt and fractures that crosscut the grain core but
392 lack diagnostic high pressure and temperature shock deformation features (Figs. 7A–C).
393

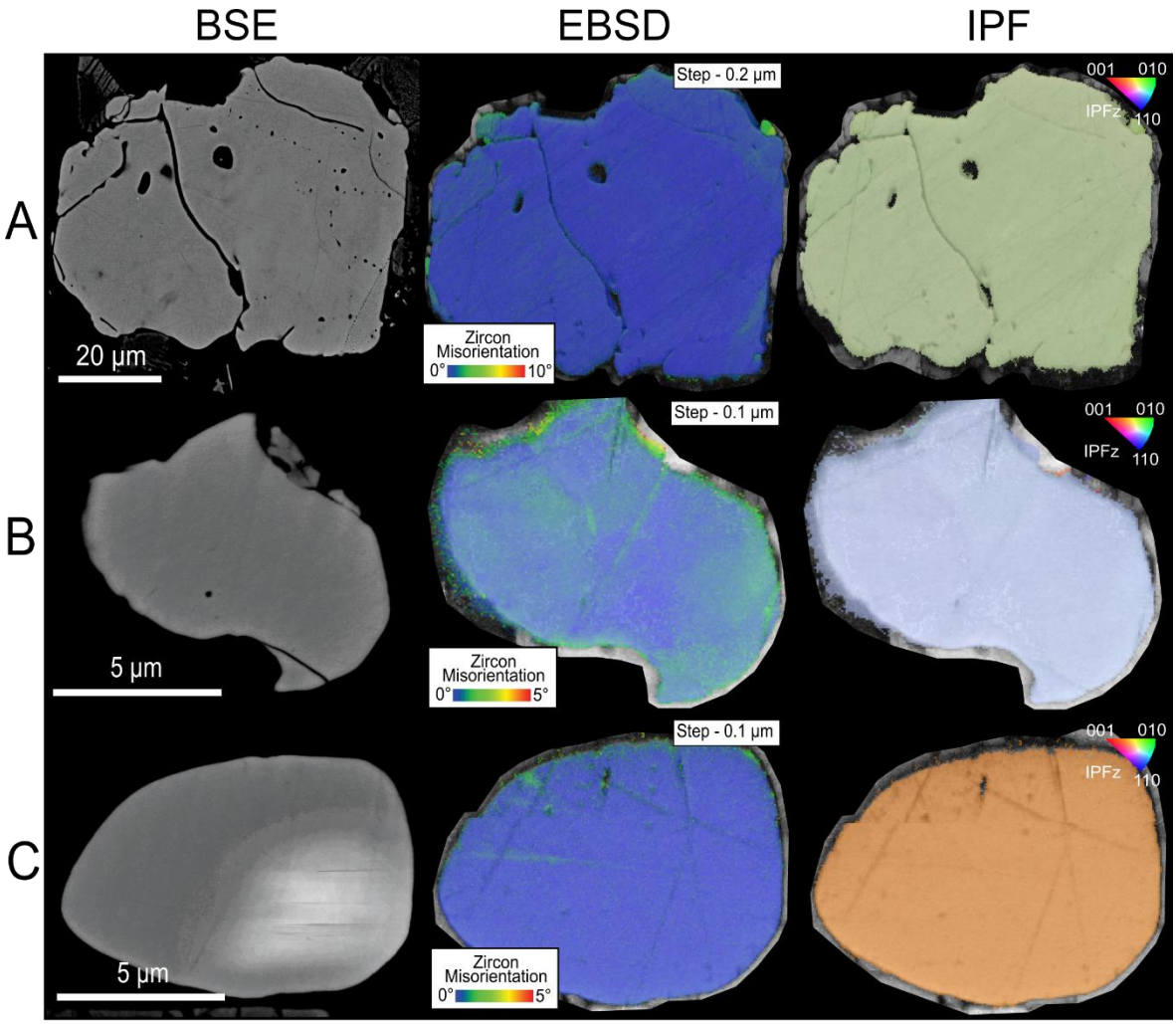

394

395 Figure 7. Overview of the zircon grain textures identified in the vesicular clast-poor melt rock
396 sample. Left column shows backscatter electron images of the grains, the center column shows
397 EBSD zircon texture component maps, and the right column shows the inverse pole figure (IPF)
398 orientations of the zircon grain acquired from EBSD analysis. (A) Subhedral zircon grain with
399 irregular fractures cross-cutting and several voids, containing the surrounding silicate melt. (B)
400 Anhedral zircon grain with partially scalloped boundaries, and a single void filled with the
401 surrounding silicate melt. (C) Zircon grain with smoothed margins showing no evidence of
402 fracturing or diagnostic shock metamorphic features. Linear markings shown in the phase and
403 EBSD orientation maps are indentations created from thin section polishing.
404

405

406

407

408 *3.2.2.2 Clast-Rich Impact Melt Rock*

409

410 Four zircon grains were identified in the clast-rich melt rock, all of which are in direct
411 contact with melt and range in size from 10 – 90 μm. They exhibit similar morphologies to the
412 grains in the clast-poor vesicular melt rock, showing no evidence of zircon dissociation or
413 diagnostic shock metamorphic features (Fig. 8). Only extensive fracturing is evident. One grain,
414 however, shows evidence of minor melt assimilation (Fig. 8A) and may have been part of a
415 larger grain that broke apart during the impact event. No evidence of zirconia crystals was found
416 along the boundary of the grain. EBSD analysis revealed no zirconia phases present, only small
417 zircon granules with orientations that differ from the main zircon grain (~20°, 0° – 5°) (Fig. 8A,
418 see Texture Component column).

419

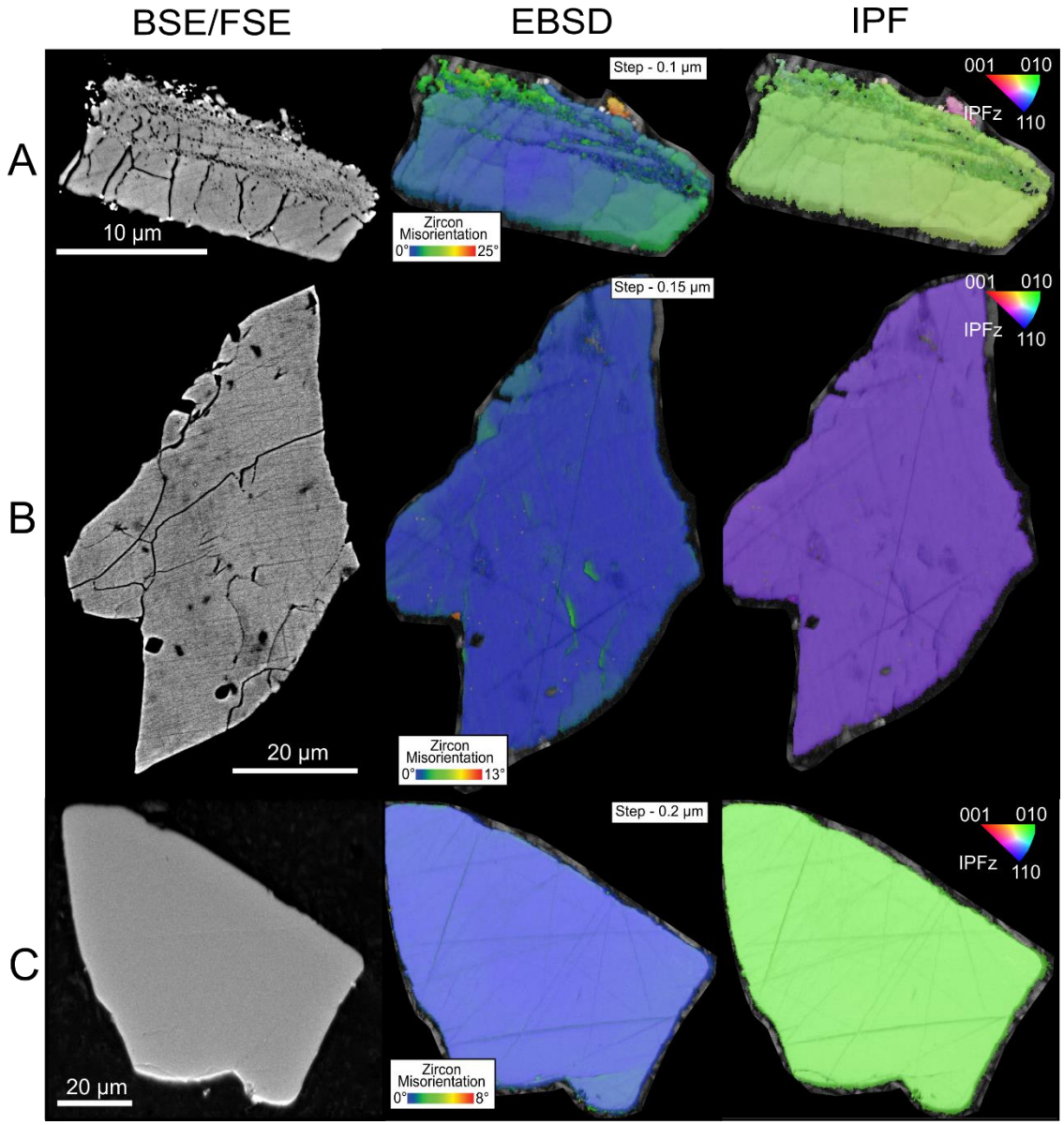

Figure 8. Overview of the zircon grain textures identified in the clast-rich melt rock sample. Left column shows backscatter electron (BSE) or forescatter electron (FSE) images of the grains, the center column shows EBSD zircon texture component maps, and the right column shows the inverse pole figure (IPF) orientations of the zircon grain acquired from EBSD analysis. (A) Zircon grain that has experienced extensive fracturing and partial thermal annealing along one margin (top of grain). No zirconia or high-pressure zircon were detected in the grain, and the smaller zircon grain fragments along the top margin exhibit different orientations compared to the large grain. (B) Anhedral zircon grain with irregular fractures cross-cutting and several voids, containing the surrounding silicate melt. (C) Zircon grain with smoothed margins showing no evidence of fracturing or diagnostic shock metamorphic features. Linear markings shown in the phase and EBSD orientation maps are indentations created from thin section polishing.

4.0 Discussion

4.1 *Zircon and Zirconia Microstructures*

In this work, we identified a collection of zircon grains and baddeleyite crystals in four impactite samples from the Mistastin Lake impact structure that record different P-T melt conditions (Fig. 9). The impact glass, where evidence for precursor cubic zirconia was discovered, records the highest superheated temperatures, >2370 °C. This is also the only impactite sample where we observe a large variation in zircon dissociation, from grains where it appears the entire original zircon grain has dissociated to silica melt and zirconia, partial dissociation around the rims of zircon grains, and also grains exhibiting no diagnostic shock deformation or dissociation (Fig. 9A). The glass-bearing impact breccia sample that was collected from an impact breccia dyke records the first evidence of both the high-pressure zircon polymorph reidite and FRIGN zircon grains at Mistastin (Fig. 9B). None of the other impactite samples contain high pressure shock metamorphic features, with the exception of the $\{112\}_{\text{zircon}}$ twinning in a single zircon grain (Fig. 3B) in the impact glass (Fig. 9A). The more crystalline impactite samples contained no diagnostic shock metamorphic features. The clast-rich and vesicular clast-poor impact melt rock samples only contained zircon grains that were fractured with crystal-plastic deformation (Figs. 9C and D). The set of observations for both of these crystalline impact melt rock samples is smaller compared to the impact glass and glass-bearing breccia (n = 4 for each crystalline impact melt rock sample). Potentially, we have not found evidence for superheating or high-P zircon microstructures in these sample because we require a greater sample abundance. Even if the crystalline impact melt rocks were no longer superheated

by the time, they reached their resting position in Mistastin they should still contain zircon grains and zirconia crystals that record evidence for superheating. To address this uncertainty in the future, a greater set of observations from crystalline impact melt rocks will be required from multiple localities in the impact structure. One scenario worth considering is whether the lack of diagnostic shock metamorphic indicators in the more crystalline impact melt samples is due to slower melt cooling rates, which may cause their annealing. Whereas the rapid quenching of the impact glass and glass-bearing impact breccia samples increases the likelihood of preserving high-P and -T shock indicators (i.e., baddeleyite crystals with high-T polymorph precursors, or reidite).

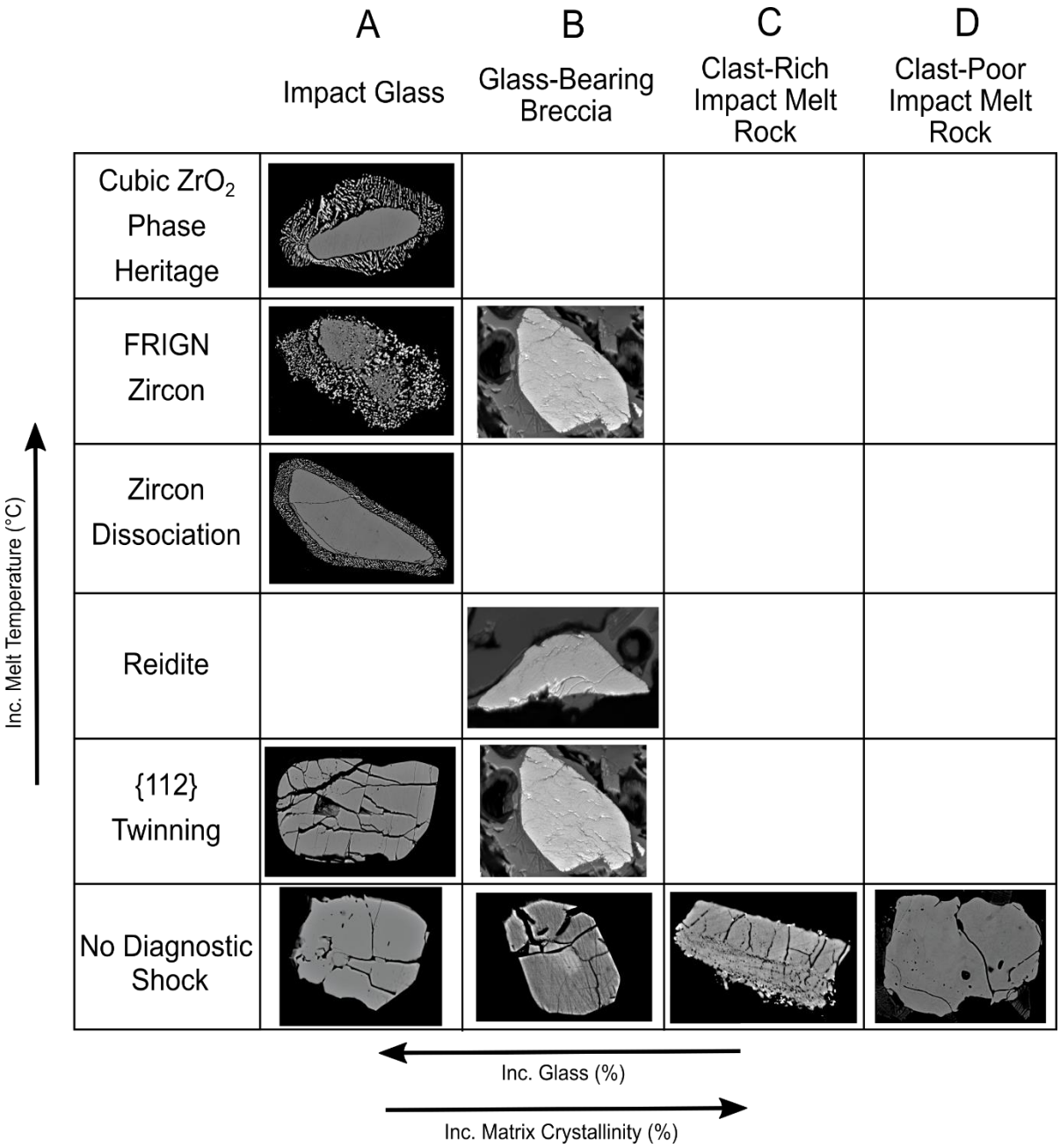

Figure 9. Summary of the zircon microstructures, diagnostic shock metamorphic features, and ZrO_2-SiO_2 dissociation products identified in the four Mistastin impactite samples. Recorded impact melt temperatures is shown to increase transitioning from medium to fine-grained crystalline impact melt samples to quenched impact glass samples. (A) Impact glass sample with the shock $\{112\}_{zircon}$ twinning, full to non-dissociated grains, and granular zircon textures. (B) Glass-bearing impact breccia from an impact breccia dyke. The zircon grains record the high-pressure polymorph reidite, granular zircon textures, and zircon grains with no diagnostic shock metamorphic features. (C) Clast-rich impact melt rock zircon grains showing no diagnostic shock metamorphic features. (D) Vesicular clast-poor impact melt rock zircon grains showing no diagnostic shock metamorphic features.

4.2 Zircon Diversity in Quenched Impact Glass

The variety of zircon shock features in the impact glass record an array of temperature and pressure conditions, revealing the P-T history of the impact cratering event. The development of shock twinning, indicated by the presence of $\{112\}_{zircon}$ twin lamellae (Fig. 3B), requires shock pressures of ≥20 GPa (Moser et al., 2011; Timms et al., 2017a, 2012), confirmed in static experiments on quenched zircon powder (Morozova et al., 2018). The lack of evident dissociation can imply two scenarios: (1) the grain was entrained into the melt when temperatures were < 1673°C (minimum temperature for zircon dissociation (El Goresy, 1965; Timms et al., 2017b; Wittmann et al., 2006)) or (2) melt temperatures were >1673°C at the time the zircon grain was entrained, but the glass rapidly quenched to <1200°C before the zircon grains experienced dissociation. The zircon grain with twinning must have originated close enough to the point of impact to be within a 20 GPa pressure contour (Melosh, 1989), but far enough from the melting zone to prevent immediate entrainment to protect the zircon grain from dissociating.

The FRIGN grain in the impact glass (Fig. 3D) would have followed the formation paths for both shock twinning and reidite, prior to being entrained into melt with temperatures >1200°C (Kusaba et al., 1985; Wittmann et al., 2006) to fully revert the reidite to zircon and produce the granular neoblastic texture (Cavosie et al., 2018; Plan et al., 2021; Timms et al., 2017a). Evidence for the former presence of reidite and shock twinning preserved in the zircon neoblast crystallographic relationships (systematic 90° disorientation alignments in $<110>_{zircon}$, and ~65° disorientations in $<110>_{zircon}$ with alignments of $<110>_{zircon}$ and $<112>_{zircon}$) indicates

that a minimum peak pressure condition of >30 GPa was achieved (Kusaba et al., 1985; Morozova et al., 2018). The presence of baddeleyite along the core boundaries and as inclusions in the grain, but lack of silica polymorphs, indicates that impact melt temperatures had to have exceeded 1687°C (Timms et al., 2017a). No evidence of the cubic to monoclinic transformation is recorded in the baddeleyite crystals, so temperatures likely did not exceed 2370°C (at ambient pressure conditions). Therefore, the reidite grain would have been entrained into impact melt with temperatures between 1687°C and 2370 °C.

Our documentation of fully, partially, and non-dissociated zircon grain textures (Figs. 3 and 9) in the impact glass sample is surprising, given the high temperature variations and time exposures to superheated melt needed to produce these textures (El Goresy, 1965; Timms et al., 2017b; Wittmann et al., 2006). For the partially dissociated zircon grains, we report two preserved temperature thresholds both recorded in baddeleyite systematic orientation relationships. The discovery of the four grains with coronas of baddeleyite that exhibit evidence of cubic to monoclinic zirconia transformation provides us with a temperature threshold between 2370 °C and 2700 °C (cubic zirconia would have melted at temperatures in excess of 2700°C (Timms et al., 2017b)). For the other 13 partially dissociated zircon grains, the crystallographic orientation relations imply that tetragonal zirconia was the high temperature polymorph, not cubic zirconia, signifying a melt temperature range of 1687 °C to <2370 °C (the lack of silica polymorphs in coronas indicates that a minimum temperature had to be at least 1687°C; (Cavosie and Koeberl, 2019; Timms et al., 2017b)).

To preserve both partially and non-dissociated zircon grain textures, one explanation is that the partially dissociated grains were entrained earlier during the opening of the transient cavity, when impact melt was still superheated. The zircon grains lacking evidence for

dissociation were likely entrained closer to the end of the impact crater formation process. At this point, impact melt temperatures were <1673°C and closer to quenching, but the viscosity of the melt had not yet reached a critical point when it could no longer entrain clasts and minerals (Onorato et al., 1978). Quenching of the glass would have needed to be rapid enough to prevent thermal annealing and erasure of the high temperature zirconia polymorph transformation orientation data, but prolonged enough to allow the melt to mix and acquire zircon grains from different locations in the transient cavity. Alternatively, the zircon grains could have spent a varied amount of time in the impact melt whilst it was superheated.

4.3 Preservation of High P-T indicators

The glass-bearing impact breccia contains the first confirmed identification of the high pressure zircon polymorph reidite (Fig. 5B) in the Mistastin Lake impact structure. This is one of the few studies to report reidite preserved in a granular zircon grain (cf. Cavosie et al., 2021; Erickson et al., 2021, 2017; Plan et al., 2021; Timms et al., 2017a), and the zircon grains containing reidite appear to have fully converted to reidite (e.g., Fig. 6). The occurrence of reidite in natural impactite samples is rare. Recent work on an impact ejecta sample from the 35 Ma Chesapeake impact structure reports a grain with 89% reidite and 11% zircon (Cavosie et al., 2021), and grains retaining 4% to 91% from a Chassenon suevitic breccia from the Rochechouart impact structure (Plan et al., 2021). Cavosie et al. (2021) report that for a near-fully converted reidite grain to form, pressure conditions would have needed to be at least 40 GPa, based off multiple shock recovery experiments (Kusaba et al., 1985; Leroux et al., 1999). Therefore, considering the amount of reidite found preserved in the glass-bearing impact breccia sample, it

546 is possible that the minimum peak pressure condition could have been as high as 40 GPa instead
547 of 30 GPa. The absence of zircon dissociation around the reidite and granular zircon grains
548 indicates that the grains were subjected to postimpact temperatures >1200 °C but <1673 °C
549 (Erickson et al., 2017; Kusaba et al., 1985; Wittmann et al., 2006). The glass in the clastic matrix
550 of the glass-bearing impact breccia was therefore at temperatures sufficient to revert reidite to
551 zircon but rapidly cooled at a rate that allowed some reidite to be retained. This is consistent with
552 the lithology of the glass-bearing impact breccia, which shows evidence for the melt quenching
553 and fragmentation during transportation, prior to intruding into fractures in the crater floor
554 (Mader and Osinski, 2018).

555 The presence of a FRIGN grain in close proximity to reidite-bearing granular zircon
556 grains in the glass-bearing impact breccia sample implies that quenching may have been
557 heterogenous. The melt surrounding the FRIGN grain must have maintained a temperature
558 >1200 °C for a longer period (Cavosie et al., 2016), allowing complete reversion of reidite to
559 zircon. The cryptic preservation of both reidite and shock twinning (90° disorientation about
560 $<110>_{zircon}$ and alignment between $<001>_{zircon}$ and $<110>_{zircon}$, 65° disorientation about
561 $<110>_{zircon}$) in the FRIGN grain indicates that the minimum shock pressure would have been ≥
562 30 GPa (Kusaba et al. 1985). Unfortunately, we cannot interpret peak pressure conditions from
563 the FRIGN grain because it is challenging to determine the state of the original zircon grain prior
564 to recrystallization. However, the systematic orientation data of the zircon neoblasts do indicate
565 that the granular zircon was not amorphous prior to recrystallization (Cavosie et al., 2021, 2016),
566 and that the grain may have been similar to the original state of the reidite-bearing granular
567 zircon; originally a massive reidite grain. After transformation to reidite, the grains would have

mixed with the melt at temperatures between 1200 °C and 1673 °C, and were emplaced as impact breccia dykes (Mader and Osinski, 2018).

4.4 *Impact Melt Thermal Evolution: Using Zircon and Zirconia*

The thermal and compositional evolution of impact melt across individual impact structures remains speculative and a topic of debate (e.g., Dence, 1971; Grieve et al., 1977; Osinski et al., 2018). By identifying an array of shock zircon microstructures and high-T parent phase precursors of zirconia from four different impactite samples at the Mistastin Lake impact structure we have demonstrated the ability to constrain impact melt evolutionary paths from different impact settings. Our observations provide evidence of superheating preserved in settings where the quenching of impact melt to glass and the rapid transportation of clastic and melt-bearing breccias along the crater floor and within shock-induced fractures (glass-bearing impact breccia) is prominent.

The preservation of both a cubic zirconia precursor in zircon dissociation corona and a FRIGN zircon core in the impact glass sample implies that the impact melt did not, however, quench at a constant rate (micron). Although the setting of the impact glass sample is unknown, we infer it to have formed at the contact between a large quartz monzonite clast and superheated impact melt (Figs. 1C and 2A,E), as we have noted chilled melt margins around large clasts in Discovery Hill impact melt exhibiting similar petrographic textures. The impact melt here would have cooled rapidly from >2370 °C to 1687 °C, and then slowly cooled to 1200 °C (as a fully crystallized FRIGN needs prolonged exposure to high temperatures). In contrast, the FRIGN

zircon grains in the glass-bearing impact breccia at the base of Mistastin's impactite stratigraphy (Fig. 2E) would have fully crystallized when exposed to superheated impact melt that had already cooled below 1673 °C. This sample would have originated from a body of impact melt (now completely eroded by glacial processes) that was deposited during the modification stage. During this stage, development of fractures into the crater floor provided a pathway for the impact melt and clastic breccia material, leading to the development of the impact breccia dyke at Steep Creek (Mader and Osinski, 2018). Upon mixing, the superheated impact melt would have rapidly cooled, but prior to that, maintained a high enough temperature to partially to fully convert reidite to a granular zircon core (> 1200 °C). The lack of zircon shock microstructures and dissociation products in the clast-rich and clast-poor impact melt rocks, which represent the thickest units at Mistastin, mark the later stages of melt evolution and impact crater development. Even though they do not record any high P-T indicators, they benchmark the point when the impact melt became chemically homogenized, as mixing would have caused the melt to reach thermal equilibrium (Marion and Sylvester, 2010; Onorato et al., 1978).

A comparison of the shocked zircon microstructures and zircon dissociation products in the four impactite samples allows us to visualize a general evolutionary pathway for the Mistastin impact melt. While these samples originate from different locations in the impact structure, they highlight just how heterogenous superheated temperature conditions and cooling durations are at the crater-scale. Each impactite sample has provided insight into how impact melt thermally evolves at different settings at Mistastin. From this, a general question arises, will we observe similar assemblages of zircon shock microstructures and dissociation products at each impact melt locality and setting across the entire impact structure, or will we observe dissimilar assemblages that record entirely different thermal evolutionary pathways? If we

observe similar zircon microstructures and baddeleyite crystals to those reported in this work at each impact melt deposit at Mistastin (see Fig. 1), then this may reflect that at the crater-scale, superheated impact melt follows a similar evolutionary pathway as it cools after emplacement. If not, these results demonstrate that the evolution of impact melt is dependent on its local emplacement process (e.g., melt pooling, flow, impact dyke injection, etc.) and proximal setting in the crater, while preservation of evidence for superheating may be highly ephemeral in comparison to the event duration of a hypervelocity impact.

Unlike Mistastin, most other terrestrial impact structures have far less preserved impact melt deposits (exceptions include large structures such as Ries, West Clearwater, Manicouagan, Sudbury, Vredefort, and Chicxulub). Therefore, it is harder to constrain thermal evolution pathways. Previous work has identified similar zircon grain and zirconia crystal samples in other impact structures (e.g., Kovaleva et al., 2021, 2019; Timms et al., 2017a), but what we discover from Mistastin is that quenched glassy impactite samples appear to record the earliest P-T conditions of the impact cratering event. The early P-T conditions are vital for understanding the excavation and modification stage of an impact crater formation event, and a majority of impact structures lack these glassy impactites capable of preserving these early P-T conditions. Melt volume does not appear to have a strong connection to the number of zircon grains and zirconia crystals, but instead correlates to the crater environment within the impact structure. Craters with preserved impact melt dykes, impact melt contacts to the crater floor/wall or large clasts, and glass, are more likely to contain the zircon and zirconia microstructures able to constrain the thermal evolutionary pathways. Terrestrial localities such as Haughton, Tunnunik, Luizi, Pantasma, and the Rochechouart are sites that can be further investigated by studying samples from impact melt dykes, ejected glass, and glass-bearing impact breccia samples. Mistastin Lake

represents a highly effective natural laboratory for constraining P-T conditions of multiple melt localities within single crater, which can in turn provide a framework for understanding other impact structures with similar settings but lacking preserved impact melt deposits.

5.0 Conclusions

We identified 69 zircon grains from four impactite samples (impact glass, clast-poor melt rock, clast-rich melt rock, and glass-bearing breccia) from the Mistastin Lake impact structure. The grains exhibit a broad range of different microstructures, levels of shock metamorphism, and dissociation. We discovered four zircon grains with evidence for the transformation of zircon to cubic zirconia in the impact glass sample, supporting work by Timms et al., (2017b) that the Mistastin impact melt was superheated to temperatures > 2370°C. In the glass-bearing breccia sample, we discovered the first evidence of reidite at Mistastin, preserved in three granular zircon grains. The fully granular zircon grain in the glass-bearing impact breccia and the granular zircon core with a corona of baddeleyite in the impact glass had crystallographic orientation relations that recorded the former presence of reidite (i.e., FRIGN zircon), and potentially superheating temperatures approaching 1673 °C.

The lack of diagnostic shock metamorphic features and zircon dissociation in the clast-rich melt rock and the clast-poor melt rock reveals the heterogeneity of temperature conditions at Mistastin, with evidence for superheating currently only found in glass-bearing impactites. However, we were only able to analyze four zircon grains from each of these two impactites, so the analysis of additional samples could lead to the discovery of finding evidence of superheating

in crystalline impact melt rocks. The occurrence of reidite-bearing granular zircon grains and FRIGN grains demonstrates that high pressure zircon polymorphs are prevalent in high temperature melt environments, helping us constrain both the high P and high T conditions during impact cratering events.

The heterogeneity in impact melt superheated temperature thresholds and the preservation of high-P zircon polymorphs shows how complex the evolution of impact melt is throughout the Mistastin Lake impact structure. Acquiring a full picture of how impact melt evolves throughout an impact structure requires the quantification of zircon and zirconia microstructures from several impact melt settings. Our results show that superheating can occur at multiple locations within an impact structure (Discovery Hill and Steep Creek), but the temperature values need not be identical, and that thicker more crystalline units preserve the point when melt becomes thermally equilibrated. We also have demonstrated that zircon microstructural and zirconia phase heritage analysis at a crater-scale can lead to a greater understanding of what the evolutionary pathways are for impact melt deposits within different settings in individual impact structures.

Acknowledgements

This work was supported by funding to GRO from the Natural Sciences and Engineering Research Council of Canada Discovery Grant and Northern Research Supplement programs and the Canadian Space Agency Flights and Fieldwork for the Advancement of Science and Technology program. Support for this research was provided in part by NASA's Planetary Science Research Program.

References

Cavosie, A.J., Biren, M.B., Hodges, K. V., Wartho, J.A., Horton, J.W., Koeberl, C., 2021. Dendritic reidite from the Chesapeake Bay impact horizon, Ocean Drilling Program Site 1073 (offshore northeastern USA): A fingerprint of distal ejecta? Geology 49, 201–205. https://doi.org/10.1130/G47860.1

Cavosie, A.J., Koeberl, C., 2019. Overestimation of threat from 100 Mt-class airbursts? High-pressure evidence from zircon in Libyan Desert Glass. Geology 47, 609–612. https://doi.org/10.1130/G45974.1

Cavosie, A.J., Timms, N.E., Erickson, T.M., Hagerty, J.J., Hörz, F., 2016. Transformations to granular zircon revealed: Twinning, reidite, and ZrO2 in shocked zircon from Meteor Crater (Arizona, USA). Geology 44, 703–706. https://doi.org/10.1130/G38043.1

Cavosie, A.J., Timms, N.E., Ferrière, L., Rochette, P., 2018. FRIGN zircon-The only terrestrial mineral diagnostic of high-pressure and high-temperature shock deformation. Geology 46, 891–894. https://doi.org/10.1130/G45079.1

Cayron, C., 2007. ARPGE: A computer program to automatically reconstruct the parent grains from electron backscatter diffraction data. J. Appl. Crystallogr. 40, 1183–1188. https://doi.org/10.1107/S0021889807048777

Cayron, C., Douillard, T., Sibil, A., Fantozzi, G., Sao-Jao, S., 2010. Reconstruction of the cubic and tetragonal parent grains from electron backscatter diffraction maps of monoclinic

zirconia. J. Am. Ceram. Soc. 93, 2541–2544. https://doi.org/10.1111/j.1551-2916.2010.03894.x

Chhabra, R.P., 2010. Non-Newtonian fluids: An introduction, in: Rheology of Complex Fluids. Springer, New York, pp. 3–34. https://doi.org/10.1007/978-1-4419-6494-6_1

Dressler, B.O., Morrison, G.G., Peredery, W. V., Rao, B. V., 1987. Shock Metamorphism features in the Sudbury Structure, Ontario, Canada - A Review, in: In: Pohl J. (Eds) Research in Terrestrial Impact Structures. Earth Evolution Sciences (International Monograph Series on Interdisciplinary Earth Science Research and Applications). Vieweg+Teubner Verlag, Wiesbaden, pp. 39–68. https://doi.org/https://doi.org/10.1007/978-3-663-01889-6_3

El Goresy, A., 1968. The opaque minerals in impactite glasses, in: Shock Metamorphism of Natural Materials. Mono Book Corp, pp. 531–553.

El Goresy, A., 1965. Baddeleyite and its significance in impact glasses. J. Geophys. Res. 70, 3453–3456. https://doi.org/10.1029/jz070i014p03453

Erickson, T.M., Kirkland, C.L., Jourdan, F., Schmieder, M., Hartnady, M.I.H., Cox, M.A., Timms, N.E., 2021. Resolving the age of the Haughton impact structure using coupled 40Ar/39Ar and U-Pb geochronology. Geochim. Cosmochim. Acta 304, 68–82. https://doi.org/10.1016/j.gca.2021.04.008

Erickson, T.M., Pearce, M.A., Reddy, S.M., Timms, N.E., Cavosie, A.J., Bourdet, J., Rickard, W.D.A., Nemchin, A.A., 2017. Microstructural constraints on the mechanisms of the transformation to reidite in naturally shocked zircon. Contrib. to Mineral. Petrol. 172, 1–26.

https://doi.org/10.1007/s00410-016-1322-0

Erickson, T.M., Timms, N.E., Pearce, M.A., Cayron, C., Deutsch, A., Keller, L.P., Kring, D.A., 2019. Shock-produced high-pressure (La, Ce, Th)PO4 polymorph revealed by microstructural phase heritage of monazite. Geology 47, 504–508. https://doi.org/10.1130/G46008.1

Farnan, I., Balan, E., Pickard, C. J., & Mauri, F. 2003. The effect of radiation damage on local structure in the crystalline fraction of ZrSiO4: Investigating the 29Si NMR response to pressure in zircon and reidite. American Mineralogist, 88, 11-12, 1663-1667. https://doi.org/10.2138/am-2003-11-1205

Gomes, R., Levison, H.F., Tsiganis, K., Morbidelli, A., 2005. Origin of the cataclysmic Late Heavy Bombardment period of the terrestrial planets. Nature 435, 466–469. https://doi.org/https://doi.org/10.1038/nature03676

Grieve, R.A.F., 1975. Petrology and chemistry of the impact melt at Mistastin Lake crater, Labrador. Bull. Geol. Soc. Am. 86, 1617–1629. https://doi.org/10.1130/0016-7606(1975)86<1617:PACOTI>2.0.CO;2

Grieve, R.A.F., Dence, M.R., Robertson, P.B., 1977. Cratering processes: As interpreted from the occurrence of impact melts, in: In Impact and Explosion Cratering: Planetary and Terrestrial Implications. pp. 791–814.

Hart, S.R., Davis, K.E., 1978. Nickel Partitioning between Olivine and Silicate Melt. Earth Planet. Sci. Lett. 40, 203–219. https://doi.org/https://doi.org/10.1016/0012-821X(78)90091-2

742 Hazen, R. M., & Finger, L. W. 1979. Crystal structure and compressibility of zircon at high
743 pressure. American Mineralogist, 64, 1-2, 196-201.

744 Kaiser, A., Lobert, M., Telle, R., 2008. Thermal stability of zircon (ZrSiO4). J. Eur. Cermaic
745 Soc. 28, 2199–2211. https://doi.org/10.1016/j.jeurceramsoc.2007.12.040

746 Kenny, G.G., Pasek, M.A., 2021. The response of zircon to the extreme pressures and
747 temperatures of a lightning strike. Sci. Rep. 11, 1–11. https://doi.org/10.1038/s41598-021-
748 81043-8

749 Kovaleva, E., Kusiak, M.A., Kenny, G.G., Whitehouse, M.J., Habler, G., Schreiber, A., Wirth,
750 R., 2021. Nano-scale investigation of granular neoblastic zircon, Vredefort impact structure,
751 South Africa: Evidence for complete shock melting. Earth Planet. Sci. Lett. 565, 116948.
752 https://doi.org/10.1016/j.epsl.2021.116948

753 Kovaleva, E., Zamyatin, D.A., Habler, G., 2019. Granular zircon from Vredefort granophyre
754 (South Africa) confirms the deep injection model for impact melt in large impact structures.
755 Geology 47, 691–694.

756 Kring, D.A., Cohen, B.A., 2002. Cataclysmic bombardment throughout the inner solar system
757 3.9-4.0 Ga. J. Geophys. Res. E Planets 107, 4–1. https://doi.org/10.1029/2001je001529

758 Kusaba, K., Syono, Y., Kikuchi, M., Fukuoka, K., 1985. Shock behavior of zircon: phase
759 transition to scheelite structure and decomposition. Earth Planet. Sci. Lett. 72, 433–439.
760 https://doi.org/10.1016/0012-821X(85)90064-0

761 Leroux, H., Reimold, W.U., Koeberl, C., Hornemann, U., Doukhan, J.C., 1999. Experimental

762 shock deformation in zircon: A transmission electron microscopic study. Earth Planet. Sci.
763 Lett. 169, 291–301. https://doi.org/10.1016/S0012-821X(99)00082-5

764 Lev, E., Hamilton, C.W., Voigt, J.R.C., Stadermann, A.C., Zhan, Y., Neish, C.D., 2021.
765 Emplacement conditions of lunar impact melt flows. Icarus 369, 114578.
766 https://doi.org/https://doi.org/10.1016/j.icarus.2021.114578

767 Lindsley, D.H., Andersen, D.J., 1983. A Two-Pyroxene Thermometer. J. Geophys. Res. 88, 887–
768 906.

769 Mader, M.M., Osinski, G.R., 2018. Impactites of the Mistastin Lake impact structure: Insights
770 into impact ejecta emplacement. Meteorit. Planet. Sci. 53, 2492–2518.
771 https://doi.org/10.1111/maps.13173

772 Marchi, S., Bottke, W.F., Bierhaus, M., Wuennemann, K., Morbidelli, A., Kring, D.A., 2014.
773 Widespread mixing and burial of Earth's Hadean crust by asteroid impacts. Nature 511,
774 578–582. https://doi.org/10.1038/nature13539

775 Marion, C.L., Sylvester, P.J., 2010. Composition and heterogeneity of anorthositic impact melt at
776 Mistastin Lake crater, Labrador. Planet. Space Sci. 58, 552–573.
777 https://doi.org/10.1016/j.pss.2009.09.018

778 Melosh, H.J., 1989. Impact Cratering: A Geologic Process. Oxford University Press (Oxford
779 Monographs on Geology and Geophysics, No. 11).

780 Melosh, H.J., Ivanov, B.A., 1999. Impact crater collapse. Annu. Rev. Earth Planet. Sci. 27, 385–
781 415. https://doi.org/10.1146/annurev.earth.27.1.385

Morozova, I., Shieh, S.R., Moser, D.E., Barker, I.R., Hanchar, J.M., 2018. Strength and deformation of zircon at crustal and mantle pressures, in: Microstructural Geochronology: Planetary Records Down to Atom Scale. pp. 167–182.

Moser, D.E., Cupelli, C.L., Barker, I.R., Flowers, R.M., Bowman, J.R., Wooden, J., Hart, J.R., 2011. New zircon shock phenomena and their use for dating and reconstruction of large impact structures revealed by electron nanobeam (EBSD, CL, EDS) and isotopic U-Pb and (U-Th)/he analysis of the vredefort dome. Can. J. Earth Sci. 48, 117–139. https://doi.org/10.1139/E11-011

Onorato, P.I.K., Uhlmann, D.R., Simonds, C.H., 1978. The Thermal History of the Manicouagan Impact Melt Sheet , Quebec. J. Geophys. Res. 83, 2789–2798. https://doi.org/https://doi.org/10.1029/JB083iB06p02789

Osinski, G.R., Grieve, R.A.F., Bleacher, J.E., Neish, C.D., Pilles, E.A., Tornabene, L.L., 2018. Igneous rocks formed by hypervelocity impact. J. Volcanol. Geotherm. Res. 353, 25–54. https://doi.org/10.1016/j.jvolgeores.2018.01.015

Osinski, G.R., Grieve, R.A.F., Marion, C.L., Chanou, A., 2012. Impact Melting, in: Osinski, G.R., Pierazzo, E. (Eds.), Impact Cratering: Processes and Products. Wiley-Blackwell, pp. 125–145. https://doi.org/10.1002/9781118447307.ch9

Osinski, G.R., Pierazzo, E., 2012. Impact Cratering Processes and Products, 1st ed. Wiley-Blackwell.

Osinski, G.R., Tornabene, L.L., Grieve, R.A.F., 2011. Impact ejecta emplacement on terrestrial planets. Earth Planet. Sci. Lett. 310, 167–181.

https://doi.org/http://dx.doi.org/10.1016/j.epsl.2011.08.012

Plan, A., Kenny, G.G., Erickson, T.M., Lindgren, P., Alwmark, C., Holm-Alwmark, S., Lambert, P., Scherstén, A., Söderlund, U., 2021. Exceptional preservation of reidite in the Rochechouart impact structure, France: New insights into shock deformation and phase transition of zircon. Meteorit. Planet. Sci. 56, 1795–1828. https://doi.org/10.1111/maps.13723

Sack, R.O., Ghiorso, M.S., 1991. Chromian spinels as petrogenetic indicators: thermodynamics and petrological applications. Am. Mineral. 76, 827–847.

Stangarone, C., Angel, R.J., Prencipe, M., Mihailova, B., Alvaro, M., 2019. New insights into the zircon-reidite phase transition. Am. Mineral. 104, 830–837. https://doi.org/10.2138/am-2019-6827

Sylvester, P., Crowley, J., Schmitz, M., 2013. U-Pb zircon age of Mistastin Lake Crater, Labrador, Canada - implications for high-precision dating of small impact melt sheets and the end eocene extinction, in: Goldschmidt. p. 2295.

Timms, N.E., Erickson, T.M., Pearce, M.A., Cavosie, A.J., Schmieder, M., Tohver, E., Reddy, S.M., Zanetti, M.R., Nemchin, A.A., Wittman, A., 2017a. A pressure-temperature phase diagram for zircon at extreme conditions. Earth-Science Rev. 165, 185–202. https://doi.org/10.1016/j.earscirev.2016.12.008

Timms, N.E., Erickson, T.M., Zanetti, M.R., Pearce, M.A., Cayron, C., Cavosie, A.J., Reddy, S.M., Wittmann, A., Carpenter, P.K., 2017b. Cubic zirconia in >2370 °C impact melt records Earth's hottest crust. Earth Planet. Sci. Lett. 477, 52–58.

https://doi.org/10.1016/j.epsl.2017.08.012

Timms, N.E., Reddy, S.M., Healy, D., Nemchin, A.A., Grange, M.L., Pidgeon, R.T., Hart, R., 2012. Resolution of impact-related microstructures in lunar zircon: A shock-deformation mechanism map. Meteorit. Planet. Sci. 47, 120–141. https://doi.org/10.1111/j.1945-5100.2011.01316.x

White, L.F., Černok, A., Darling, J.R., Whitehouse, M.J., Joy, K.H., Cayron, C., Dunlop, J., Tait, K.T., Anand, M., 2020. Evidence of extensive lunar crust formation in impact melt sheets 4,330 Myr ago. Nat. Astron. 4, 974–978. https://doi.org/https://doi.org/10.1038/s41550-020-1092-5

White, L.F., Darling, J.R., Moser, D.E., Cayron, C., Barker, I., Dunlop, J., Tait, K.T., 2018. Baddeleyite as a widespread and sensitive indicator of meteorite bombardment in planetary crusts. Geology 46, 719–722. https://doi.org/10.1130/G45008.1

Wittmann, A., Kenkmann, T., Schmitt, R.T., Stöffler, D., 2006. Shock-metamorphosed zircon in terrestrial impact craters. Meteorit. Planet. Sci. 41, 433–454. https://doi.org/10.1111/j.1945-5100.2006.tb00472.x